Computations of Axisymmetric Flows in Hypersonic Shock Tubes

Surendra P. Sharma and Gregory J. Wilson

Computations of Axisymmetric Flows in Hypersonic Shock Tubes

Surendra P. Sharma*
NASA Ames Research Center, Moffett Field, California 94035
and
Gregory J. Wilson†
Thermosciences Institute, Moffett Field, California 94035

A time-accurate two-dimensional fluid code is used to compute test times in shock tubes operated at supersonic speeds. Unlike previous studies, this investigation resolves the finer temporal details of the shock-tube flow by making use of modern supercomputers and state-of-the-art computational fluid dynamic solution techniques. The code, besides solving the time-dependent fluid equations, also accounts for the finite rate chemistry in the hypersonic environment. The flowfield solutions are used to estimate relevant shock-tube parameters for laminar flow, such as test times, and to predict density and velocity profiles. Boundary-layer parameters such as δ_u, δ^*, and τ_w, and test time parameters such as τ and particle time of flight t_f, are computed and compared with those evaluated by using Mirels' correlations. This article then discusses in detail the effects of flow nonuniformities on particle time-of-flight behind the normal shock and, consequently, on the interpretation of shock-tube data. This article concludes that for accurate interpretation of shock-tube data, a detailed analysis of flowfield parameters, using a computer code such as used in this study, must be performed.

Nomenclature

a = speed of sound, m/s
C_p = specific heat ratio
d, D = shock-tube diameter, m
L = length of driven section, m
l = distance downstream of the shock front, 0 at shock front, l_c at contact surface, m
$l_{c,m}$ = maximum separation between the shock front and the contact surface, m
$\dot{m}$ = mass flow, kg/m^3
P = pressure, N/m^{-2}
T = translational temperature, K
t_f = particle time of flight, $\int_0^{l_c} (\rho_e/\rho_x U_s)\, dl$, s
U_s = shock front velocity in the laboratory coordinates (wall stationary), m/s
u = flow velocity in shock stationary frame, m/s
W = $u_w/u_{e,0} = \rho_{e,0}/\rho_x$
X = nondimensional axial distance, $u_{e,0}t/l_{c,m}$, $t = \int_0^{l} dl/u_e$
y = radial coordinate, 0.0 at tube center, m
β = constant
δ^* = displacement thickness, $\int_0^{\infty} (u\rho - u_e\rho_e)/(u_e\rho_e)_0\, dy$, m
δ_u = boundary-layer thickness based on velocity, y at $(U_s - u)/(U_s - u_e) = 0.99$, m
δ_ρ = density displacement thickness, $\int_0^{\infty} (\rho/\rho_e - 1)\, dy$, m
μ = coefficient of viscosity, kg/m s
ρ = density, kg/m^3
τ = test time at $l = l_c$, l_c/u_w, s
τ_x = test time at $l = l_{c,m}$, $l_{c,m}/u_w$, s

$\bar{\tau}$ = nondimensional test time, τ/τ_x
χ = h_w/h_c

Subscripts
c = contact surface
e = downstream of the shock front
$e, 0$ = immediately behind the shock front
m = limiting flow regime
s = shock
st = standard conditions, 1 atm, 294 K
u = velocity
w = wall
1 = upstream of shock front
2 = conditions between shock front and contact surface
∞ = upstream of the shock front

I. Introduction

SHOCK tubes, by producing high-temperature gases, provide a very powerful tool[1-4] for the study of gases at temperatures beyond those obtainable in furnaces. The shock tubes produce a homogeneous gas sample with enthalpy and pressure that can be dependably and literally calculated from the measured shock velocity and the conservation laws. It is this dependable, accurate production of gas samples that makes shock tubes a most attractive tool for high-temperature research. Under ideal conditions, such as a flow without wall or real-gas effects, the shock wave and contact surface would move with a constant velocity and the flow between them is uniform and one dimensional. However, in a real shock tube the homogeneity of the gas sample produced begins to suffer as the boundary layer grows and as real-gas effects become important. The interface between the driver gas and driven gas sample is typically turbulent. This turbulent region, along with boundary-layer effects and other complexities, usually engulfs a significant part of the heated driven gas, in some cases up to half of the total driven gas. When the separation between the contact surface and the shock front is larger than one tube diameter, a large portion of the heated gas sample is unaffected by the turbulent contact surface.[5] In these large tubes, this region is typically homogeneous with a planar shock

front. The achievement of a planar shock front followed by a homogeneous gas sample is essential for the validity of the conservation laws and the accuracy of the gas state calculations. The interpretation of shock-tube data measured in this homogeneous test gas sample is straightforward, since the time of flight of the particles participating in the thermokinetic processes is accurately predictable.

However, as the length-to-diameter (L/D) ratio of the driven section is increased and as the initial pressure in it is reduced, the wall boundary-layer effects become more pronounced. The flow nonuniformities between the shock front and the contact surface add further complexities to the boundary-layer effects. The separation between the contact surface and the shock front l_c increases with an increase in L/D until it reaches a maximum, at which point a limiting flow is established. At this point the shock and the contact surface move with a constant velocity. Duff,[6] to explain the limiting flow, referred to the contact surface as a leaky piston, such that a fraction of the test gas leaks through the wall boundary layer. He explained that the limiting flow occurs when the flow through the shock front is equal to this leakage. Roshko[7] and Hooker[8] later studied this effect both experimentally and theoretically. Based on the experimental data, Roshko was able to confirm the validity of the basic theory. Analytical studies by Roshko,[7] subsequently expanded and modified by Hooker,[8] are primarily based on the computations of boundary-layer parameters such as δ_u, δ^*, etc., in terms of relevant shock-tube operational parameters, such as $W \equiv u_w/u_{e,0} = \rho_{e,0}/\rho_x$, the shock strength parameter P_2/P_1, the pressure ratio across the shock, and the shock Mach number. Using the boundary-layer parameters, the incoming mass across the shock and outgoing fluid mass across the contact surface can be estimated. In the limiting flow case when the incoming mass is equal to the outgoing mass across the contact surface, it is possible to derive a set of equations, which can be solved to compute the $l_{c,m}$ and other relevant test time parameters. Roshko[7] used a simplified model assuming that 1) the contact surface moves with a constant velocity and 2) the freestream has a uniform velocity profile. Later, this model was modified by Mirels[9-14] to account for the acceleration of the contact surface, flow nonuniformities, and real-gas effects.

Comparisons with available experimental data in all of these investigations were limited to shock velocities below 2.0 km/s. In the early 1960s, Kemp[15] extended these models for higher velocities (6.0–10.0 km/s) and found that the actual measured test times for these velocities were, on average, one order of magnitude smaller than the values predicted by this theory. Kemp pointed out that this discrepancy may be caused by some additional phenomena not accounted for in these models, such as mixing and density gradient instabilities at the contact surface, and the predicted values should be regarded as the upper limit of the test time that can be achieved in a shock-tube facility.

In these early analyses the separation between the surfaces, in distance or time, was taken to be as a measure of test time. However, the early experimentalists and developers[2-5] of low-density shock tubes did realize that the entire separation length is not filled with a homogeneous gas. Kantrowitz[5] thought that the homogeneous portion would account for only one-half of the separation length, or even less, as the gas temperature is increased.

Since most of the shock-tube data relate to the kinetic processes in the test gas sample, the experimentalist must evaluate the time required for a shock-heated particle to reach a specified distance downstream of the shock front for proper interpretation of the data. If the conditions behind the shock front are uniform, then the time of flight of a given particle, at a distance l from the shock front, is equal to

$$t_f = (\rho_{e,0}/\rho_x)(l/U_s)$$

Here, $\rho_{e,0}$ and ρ_x are the densities immediately downstream and upstream of the shock front, respectively. In a nonuniform flow case

$$t_f = \int_0^l \left(\frac{\rho_e}{\rho_x}\right) \frac{dl}{U_s}$$

Mirels' computations[14] show that in the limiting flow case a particle may take about four times longer time to reach a distance $l = 0.9l_{c,m}$ than predicted by the uniform flow case. Thus, in order to interpret the shock-tube data correctly, the experimentalist must have accurate knowledge of the flowfield behind the shock front.

These findings are not new and over the years, many authors, notably Mirels, have written numerous papers to this subject. However, both experimental and theoretical investigations of the homogeneity of the test gas sample are difficult to conduct and, for that reason, many investigators tend to ignore these phenomena when interpreting the shock-tube data.

In this article the authors revisit the problems associated with inhomogeneity of the test gas in shock tubes using state-of-the-art computational fluid dynamic (CFD) techniques. Taking advantage of modern supercomputers and CFD techniques, we are able to resolve the finer details of the boundary layers and are able to computationally model the complexities of finite rate chemistry and thermal nonequilibrium. In the present computational study we have obtained the flowfield solution for a low-density operating condition with a laminar boundary layer, for which the assumptions made by Mirels are valid, namely, 1) modest real-gas effects $T_2 \sim 3500$ K, 2) low Mach number $M_s \sim 8$, and 3) cold wall $T_w = 294$ K. At first we will compare our computational results of separation length (test time) with those based on Mirels' correlations and experimental data of Camm et al.,[4] Duff,[6] Hooker,[8] Roshko,[7] Wuster et al.,[15] and Sharma et al.[16] Then we will discuss the homogeneity of the test gas sample by examining in detail the computed flowfield profiles and its impact on the particle time of flight and, consequently, on the interpretation of the shock-tube data. Finally, we will assess the role of this new computational tool in assisting the experimentalists in interpretation of shock-tube data.

II. Mirels' Correlation Formulas for Shock-Tube Flow

First, we describe the basic features of boundary-layer developments in a shock tube, although they have been presented by Mirels and others[6-12] in numerous publications. The shock-tube flow, as discussed by Mirels, is viewed in a coordinate system in which the wall moves with a velocity u_w (which equals U_s in the laboratory coordinate system, Fig. 1). In this shock stationary system the local flow parameters between the shock front and the contact surface are denoted by subscript e and the values directly behind the shock are de-
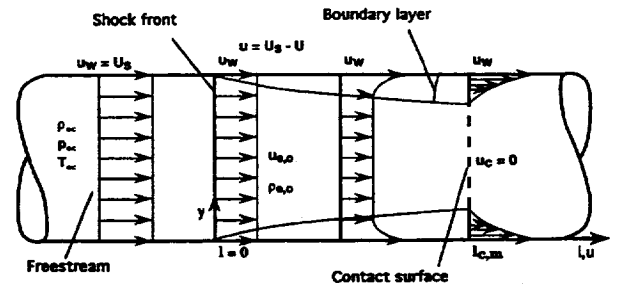

Fig. 1 Shock-tube flow in shock stationary coordinates; u and U are the velocities in the shock stationary and laboratory coordinates, respectively.

noted by an additional subscript 0. The contact surface is located at a distance l_c from the shock front. The conditions upstream of the shock front are denoted by subscript ∞ and the conditions at the wall by subscript w.

Duff's leaky piston analogy can be visualized by examination of the sketch in Fig. 1. The mass flow through the shock front $\dot{m}_s$ can be expressed by

$$\dot{m}_s = (\rho_c u_c)_0 A = \rho_\infty U_s A \qquad (1)$$

where A is the cross-sectional area of the shock tube. If it is assumed here that the boundary layer is thin compared to the tube diameter, the leakage at the contact surface is given by

$$\dot{m}_c = L\rho_{w,0}(u_w - u_{c,0})\delta \qquad (2)$$

where L is the perimeter of the tube, δ is the characteristic boundary-layer thickness at l_c (see Fig. 1), and $\rho_{w,0}$ and $u_w - u_{c,0}$ are the boundary-layer density and velocity, respectively. The added momentum due to the excess mass $\Delta\dot{m} = \dot{m}_s - \dot{m}_c$ causes the acceleration of the contact surface as observed in many experiments.[13] In the limiting flow ($l = l_{c,m}$, $\Delta\dot{m} \sim 0.0$), the in-flow through the shock front is equal to the mass leakage through the contact surface. The condition $\dot{m}_s = \dot{m}_c$ provides a unique relationship between the shock-tube parameters and the boundary-layer parameters at $l = l_{c,m}$ and the maximum separation length $l_{c,m}$ itself.

For a laminar flow the characteristic boundary-layer thickness, δ at $l = l_{c,m}$, can be written as[11]

$$\delta = \beta \left[\frac{\mu_{w,0} l_{c,m}}{\rho_{w,0}(u_w - u_{c,0})} \right]^{1/2} \qquad (3)$$

Here, the β is a constant that must be determined. Assume that the temperature upstream of the shock front is at a standard condition so that $T_\infty = T_{st}$, $a_\infty = a_{st}$, and $\mu_\infty = \mu_{st}$. It is further assumed that the wall remains at the initial temperature, i.e., $T_w = T_{st}$. For most of the shock-tube operations this assumption is valid.[12]

Equations (1–3) can be combined to yield

$$\frac{p_{st}}{p_\infty} \frac{l_{c,m}}{d^2} = \frac{1}{16\beta^2} \left(\frac{p_\infty}{p_{c,0}} \frac{WM_s}{W-1} \right) \left(\frac{\rho a}{\mu} \right)_{st} \qquad (4)$$

Here, $W \equiv u_w/u_{c,0} = \rho_{c,0}/\rho_\infty$ and $M_s = U_s/a_\infty$ is the shock Mach number.

Equation (4) can be used to compute the maximum achievable separation distance $l_{c,m}$, however, it requires an accurate estimate of β. Numerous schemes for computations of β have been proposed over the years[6,7,11,13] varying in level of intricacy. Mirels,[11] using the local similarity approximation based on the computation of displacement thickness, has proposed the following expression:

$$\beta = 1.59C_c^{0.37} \left(1 + \frac{1.796 + 0.802W}{ZW - 1} \right) \quad C_c \equiv \frac{\rho_c \mu_c}{\rho_w \mu_w}$$

$$= \frac{1}{z_2} \frac{T_1}{T_2} \frac{\mu_2}{\mu_1}, \qquad z_2 = \frac{P_2}{\rho_2 RT_2} \qquad (5)$$

Here, C_c is the correction factor for variable $\rho\mu$.[9] $Z = (\gamma + 1)/(\gamma - 1)$ for an ideal shock. The expression for the constant β [Eq. (5)] includes the effects of freestream nonuniformities.[11] Mirels recommends that for a strong nonideal shock Z be replaced by W ($W \geq Z$). For a shock Mach number greater than 8 the error caused by replacing Z with W is less than 1%. In this study, we have used Eqs. (4) and (5) to compute $l_{c,m}$. Other correlations that were used to estimate various boundary-layer parameters are included in the Appendix. These correlations are from Ref. 12 and are valid for variable $\mu\rho$,

however, they assume a constant freestream between the shock front and the contact surface.

III.   Fluid Flow Model

As mentioned in Sec. I, the present study is based on an axisymmetric flowfield simulation of the shock-tube flow. A detailed description of this code has been presented elsewhere.[17] However, for completeness, its basic features are given in the following text.

Fluid flow through the shock tube is modeled by coupling the thin-layer, Navier–Stokes equations with chemical reaction rate equations. The gas model includes the three major species (N_2, N, and He) and accounts for finite rate chemical processes. A separate equation for vibrational energy is included, but thermal equilibrium is enforced for the present work. Species diffusion effects are not included. The problem is assumed to be axisymmetric. The contact discontinuity is initially assumed to be planar and the boundary layer is treated as laminar. The equations are solved to provide a time-accurate solution. As a result, the temporal evolution of boundary-layer growth, mass leakage through the boundary layer, acceleration of the contact surface, and deceleration of the shock front can be monitored.

IV.   Numerical Method

The axisymmetric gasdynamic equations are solved by using an explicit finite volume form of the Harten–Yee upwind total variation diminishing (TVD) scheme,[18] which gives second-order spatial and temporal accuracy. The simulations cluster grid points at the shock and contact discontinuity and convect this clustered grid with these features as they travel down the driven tube to minimize numerical errors.

The solutions are advanced at a Courant–Friedrichs–Lewy (CFL) number less than one based on the inviscid gasdynamics. In the boundary layer, this CFL number can be significantly larger than the stability bound required by the viscous terms. To avoid the limiting time step dictated by the viscous terms, these terms are treated implicitly. This requires a block tridiagonal matrix inversion along each line of cells normal to the wall. The cost of this inversion is more than offset by the greater allowable time step. The source terms representing the finite rate chemical kinetics and vibrational relaxation are also treated implicitly. This implicit treatment reduces the formal time accuracy to first order.

V.   Results

Numerical results generated by this code have been compared against experimental data and were reported.[17] The experimental data were obtained at NASA Ames' Electric Arc-Driven Shock-Tube Facility.

A.   Computed Flowfield

The shock-tube geometry used in the present study had a driver of 0.76 m in length and a driven tube of 12.00 m in length with 0.05 m i.d. The single run condition investigated had a driven tube fill pressure of $p_\infty = 0.525$-torr nitrogen at 294 K. The driver pressure and temperature were 6.93 atm and 700 K, respectively. The axial distance was divided into 400 grid points and the radius into 63 grid points. The radial grid system was clustered at the wall to provide better resolution of the boundary layer. The grid in the axial direction was clustered near the shock front and the contact surface.

To ascertain that the computational results are grid independent, a grid convergence analysis was conducted. The minimum grid size at the wall was reduced in four consecutive runs, from 50.0 to 6.25 μm and the resultant flowfields were compared. All runs were started at the point in time when the diaphragm ruptures and carried through the point of (or very close to) limiting flow. The point of limiting flow was determined by plotting the value of l_c as a function of time
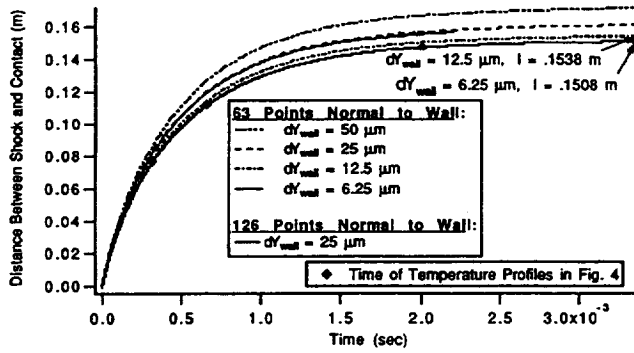
Fig. 2 Separation distance between the shock front and the contact surface, *l* as a function of time.
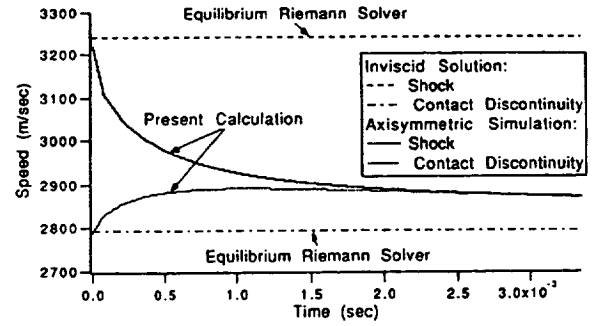

Fig. 3 Shock-front and contact surface speeds as functions of time in laboratory coordinates.

Fig. 4 Translational temperature as functions of axial distance in laboratory coordinates.

and by monitoring the value l_c in time. It was assumed that limiting flow was achieved when l_c remained constant with further increase in time. The results of the four computations are shown in Fig. 2. The $l_{c,m}$ value changed by 6.4% when the grid size at the wall was reduced from 50 to 25 μm. The change in $l_{c,m}$ value was about 4.4% when the grid size was changed from 25 to 12 μm. The difference between the $l_{c,m}$ values for grids with 6.25 and 12.5 μm was found to be only 2%. The displacement thickness, which is at the heart of Mirels' theory for boundary-layer parameters and test times in shock tubes, was also found to be within 2% for these two cases. At this point 6.25-μm grid size at the wall was selected as the final grid. For the final grid, the cell Reynolds number at the wall as defined by the following relationship was found to be 3.5 at the shock front decreasing to 0.6 at the contact discontinuity:

$$Re_{cell} = \frac{\rho_w u_{cell} \Delta y}{\mu_w}$$

Here, u_{cell} is the velocity at the center of the first cell above the wall and Δy is the height of the first cell above the wall. As a rule of thumb, Re_{cell} must be less than one to achieve an acceptable resolution of the boundary layer. With $Re_{cell} = 0.6$ at the contact discontinuity, we are confident that the boundary layer is sufficiently resolved. However, since the boundary layer is thinner near the shock front, it is less resolved in this region. This is revealed by the value of $Re_{cell} = 3.5$ behind the shock. Consequences of this fact will be discussed later. To ensure that the 63 points used across the radius of the tube were sufficient, an additional computation with the 25-μm wall spacing was made using 126 points across the radius. The results of this run are also presented in Fig. 2. This run was not carried out as far as the other computations, but shows little difference from the 63-point solution. The code requires 12.2-μs/grid point/iteration on a Cray C-90. The final solution with the 6.25-μm spacing at the wall was run for 760,000 iterations, requiring approximately 65 h of CPU time. This computation was the most expensive, since the time step size is controlled by the wall spacing.

Also marked in Fig. 2 are four points corresponding to separation lengths of 0.5, 0.75, 0.96, and $\approx l_{c,m}$ for the finest grid solution. The first point is reached in 0.32 ms after diaphragm rupture, the second in 0.66 ms, the third in 2.01 ms, and the fourth at 3.35 ms. These four points will be referred to later. Mirels' correlations predict $l_{c,m} = 0.152$ m, about 0.8% higher than the value of 0.1508 m based on our final solution ($t = 3.35$ ms). It is conceivable that if the code were allowed to run further, the computed value of $l_{c,m}$ may reach Mirels' value, however, it would more than double the integration period and was deemed impractical for this study.

The shock front and contact surface velocities (in the laboratory coordinates) as a function of the time from diaphragm rupture are shown in Fig. 3. The deceleration of the shock
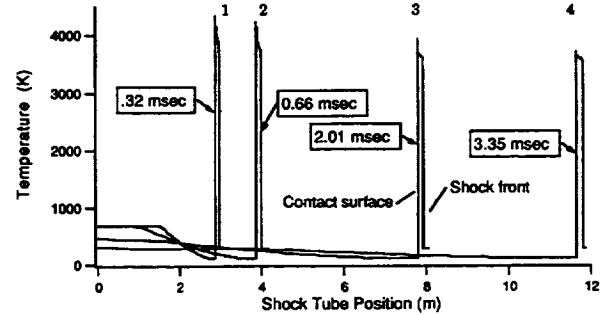
front and acceleration of the contact surface are clearly seen in this figure. Because of the large deceleration of the shock front, the particles passing through the shock in the early stages of the flow are processed by a shock whose strength is significantly greater than its strength at later times. This phenomenon causes additional inhomogeneity in the test gas sample, besides those due to the boundary-layer effects discussed earlier.

The temperature profiles over the whole shock tube are shown in Fig. 4. Plots for the four points indicated in Fig. 2 are shown in Fig. 4. For clarity, the plots on Fig. 4 are shown in the laboratory coordinates. Two observations are made here:

1) The difference between the temperatures directly downstream of the shock front and at the contact surface is much larger at point no. 1 ($l_c = 0.5 l_{c,m}$, $\Delta T \approx 458$ K) than that at point no. 4 ($l_c \approx l_{c,m}$, $\Delta T \approx 153$ K).

2) A large temperature gradient exists upstream of the contact surface at point no. 1, which as the shock moves further along the driven tube, almost disappears at $l_c = l_{c,m}$. The translational temperature at the contact surface at point no. 1 is about 4300 K, as compared to 3842 K at the shock front. Fluid particles at the contact surface were processed before those at the shock front, and as seen from Fig. 3, therefore processed by a stronger shock. The temperature of 4300 K at the contact surface at point no. 1 is consistent with the post-shock temperature for the initial shock speed of 3200 m/s. As the gas sample moves along the shock tube some of the fluid particles at the contact surface leak out through the boundary layer, resulting in a slightly cooler contact surface at later times (see point no. 4 in Fig. 4).

Velocity contours corresponding to the limiting flow solution are shown in Fig. 5, which clearly shows the shock front, contact surface, and the boundary-layer buildup. Each contour in this figure represents a 30-m/s change in velocity. The flow streamlines in the shock fixed coordinates are shown in Fig. 6. It is very instructive to see that, this being the limiting flow, all of the streamlines (and the mass flow through them) at the contact surface flow into the confines of the boundary
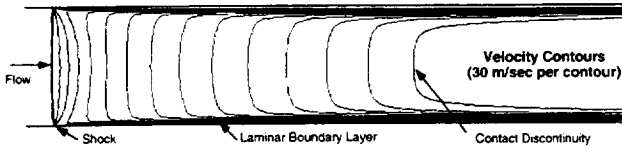
Fig. 5 Velocity contours in the test gas sample; $P_\alpha = 0.525$ torr, T_α = 294 K, and d = 0.05 m. Driver: T = 700 K and P = 6.93 atm. Shock stationary coordinates.
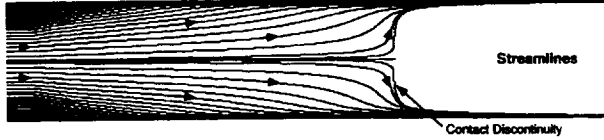

Fig. 6 Streamline contours in the test gas sample; $P_\alpha = 0.525$ torr, T_α = 294 K, and d = 0.05 m. Driver: T = 700 K and P = 6.93 atm. Shock stationary coordinates.
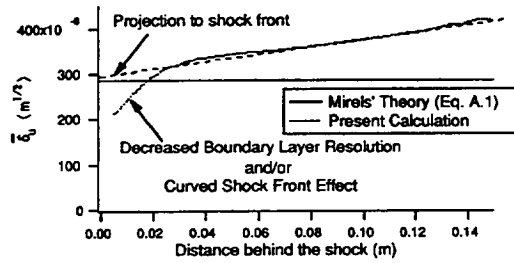

Fig. 7 Boundary-layer thickness parameter as a function of distance measured from the shock front.

layer. This clearly demonstrates the leaky piston analogy of Duff, as was mentioned earlier. Since no experimental verification of the leaky piston concept has been produced, it is instructive to visualize and demonstrate leaky piston phenomena using the present code, supporting the theories of Mirels, Duff, and Roshko.

B. Mirels' Theory vs Present Analysis

One of the most interesting relationships that appeared in Mirels' work was the universal relationship between the nondimensional maximum shock/contact surface separation distance and the shock Mach number. Mirels' universal relationship is based on several other parameters, such as, δ_u, δ^*, δ_ρ, τ_w, $\dot{q}_w$, and other shock-tube parameters, such as τ and X along the driven length. The expressions for the boundary-layer parameters are listed in the Appendix. The test time parameters are defined as follows:

$$\bar{\tau} = \frac{\tau}{\tau_x}, \quad \tau = \frac{l_c}{u_w}, \quad \tau_x = \frac{l_{c,m}}{u_w}, \quad X = \frac{u_{e,0}l}{l_{c,m}}, \quad t = \int_0^{l_c} \frac{dl}{u_e} \quad (6)$$

The δ_u for the limiting flow, based on Mirels' correlation as well as from the present study, is plotted in Fig. 7. The value based on Mirels' correlation is constant over the distance since the correlations assume a uniform freestream ($u_e = u_{e,0}$). However, since in the present solution the freestream conditions are changing as a function of distance, the computed boundary-layer parameters do not remain constant over the distance l_c between the shock front and the contact surface. Ideally, the values of these parameters from both sets should be the same at l = 0.0, immediately behind the shock front. However, at l = 0.0 the boundary layer is very thin and, even with the grid size of 6.25 μm at the wall, it is not possible to resolve the boundary-layer parameter near the shock front accurately. Also, the shock front tends to be curved near the wall and the resultant freestream near the wall has its own effect on the boundary-layer growth. For these reasons, the values of the boundary-layer parameters do not agree with

Table 1 Values for $l = 0.9l_{c,m}$ **at limiting flow regime**[a]

	Present study	Mirels' data	Difference, %
δ_u	4.04e$-$4	2.85e$-$4	41.7
δ^*	8.74e$-$4	7.03e$-$4	24.3
δ_ρ	9.03e$-$5	7.87e$-$5	14.7
$\bar{\tau}_w$	2.02e$+$3	2.00e$+$3	1.0
$\dot{q}_w$	6.02e$+$6	6.27e$+$6	4.0

[a]Here, δ_u, δ^*, and δ_ρ are in the units of m$^{1/2}$, $\bar{\tau}$ is in the units of N m$^{-3/2}$, and $\dot{q}_w$ is in the units of W m$^{-3/2}$.
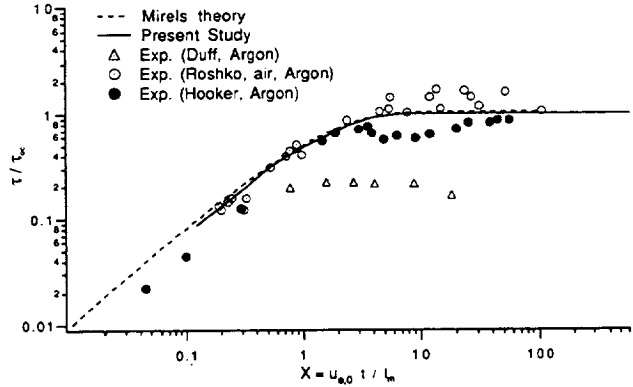

Fig. 8 Nondimensional test time as computed and based on Mirels' correlations compared with experimental data; $U_s < 3.0$ km/s.
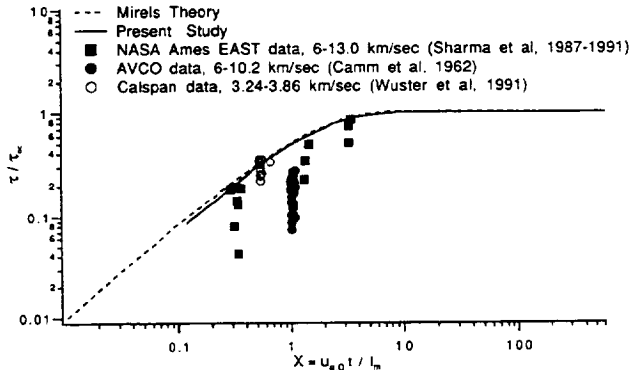

Fig. 9 Nondimensional test time as computed and based on Mirels' correlations compared with experimental data; $U_s > 3.0$ km/s.

Roshko's and Hooker's data show reasonable agreement with the theoretical curves, especially the asymptotic nature of $\bar{\tau}$. Roshko used the value of $\beta = \sqrt{3}$ in analyzing his data. The the values based on Mirels' correlations at l = 0.0. If the results for $l > 0.08$ m, where the boundary layer is well resolved, are extrapolated (see Fig. 7) to the shock front, then the agreement is good. It should be noted that the effect of nonuniform freestream on δ_u is particularly significant (see Table 1).

For computing $\bar{\tau}$, $l_{c,m}$ was computed using Eqs. (4) and (5). The computed value of $l_{c,m}$ is 0.1508 m against 0.1519 m based on Mirels' correlations (a difference of 0.7%). As mentioned earlier, Mirels' correlations for $l_{c,m}$ are corrected for the nonuniformities in the freestream and the correlations for δ^*, etc., are not. That is why, in spite of a significant difference in the values of the boundary-layer parameters, especially δ^*, there is an excellent agreement in the values of $l_{c,m}$. It is not surprising that a plot of $\bar{\tau}$ vs X using Mirels' theory also shows an excellent agreement with the present computations (Fig. 8). Also shown on the plots are the experimental data of Duff,[6] Roshko,[7] and Hooker[11] reproduced from Ref. 11.

parameter $\bar{\tau}$ is very sensitive to the value of β near its asymptotic value ($\bar{\tau} \sim 1.0$). If β were correctly evaluated Roshko's data should be asymptotic, i.e., $\bar{\tau} \rightarrow 1.0$ (since $l_{c,m} \propto \beta^{-2}$). It should be noted that all of the experimental data plotted in Fig. 8 are for $M < 9$ and the present computations are for $M = 8.2$.

As mentioned earlier, at higher velocities the flowfields are affected by some additional phenomena[13] not accounted for in the present code or in Mirels' correlations, such as mixing and thermal instabilities. As a result the recorded test times are much smaller than those predicted by the theory. Sometimes these instabilities cause the disintegration of the contact surface and under these conditions it is difficult to make any reliable measurement of the test time. A plot of test times at higher velocities from the experimental data of Sharma et al.,[16] Wuster et al.,[15] and Camm et al.[4] is shown in Fig. 9 along with the theoretical predictions. For computing $\tau_\infty = l_{c,m}/u_w$, $l_{c,m}$ for all of the experimental data plotted in Fig. 9 was taken from Mirels' computations (Ref. 11, Fig. 6). In the present simulation, for simplicity, assume a clean "breakup" of the diaphragm, which is rarely the case. Also, it is difficult to simulate the shot-to-shot variations caused by minute imperfections in driver assembly, such as diaphragm defects, trigger wire geometry, fill gas pressures, etc. Experience[16] shows that these unavoidable imperfections affect the way the diaphragm opens and in certain cases cause the onset of various interface instabilities. These phenomena are reflected in the test data presented in Figs. 8 and 9. In view of these facts one concludes that the theoretical curves provide only the upper limit for the test time, and in real shock tubes the test time is usually smaller.

In summarizing the results for laminar flow with relatively small real-gas affects, Mirels' universal correlations provide good estimates of the test times. The accuracy of these predictions is comparable with that achieved by using an intricate tool such as the present fluid code. However, the boundary-layer thickness is very sensitive to the flow nonuniformities and only a computer code such as is presented here or detailed experimental measurements can provide the needed information about it.

C.   Test Gas Homogeneity

Figure 10 depicts the relative variation of various thermodynamic parameters, namely, T, P, and u_c, with respect to their magnitude at the shock front (T_s, P_s, and $u_{c,0}$), as a function of normalized distance from the shock front, $l/l_{c,m}$. The properties shown correspond to the limiting flow regime ($l = l_{c,m}$). The flow velocity in the shock stationary coordinates reduces to 0.0 as a particle moves towards the contact surface, which is as expected in the limiting flow case. The changes in temperature and pressure are less dramatic. Pressure increases by 9.5% and the temperature by 4.8%. Figure 11 shows the variation of these properties at a location when the separation between the contact surface and shock front
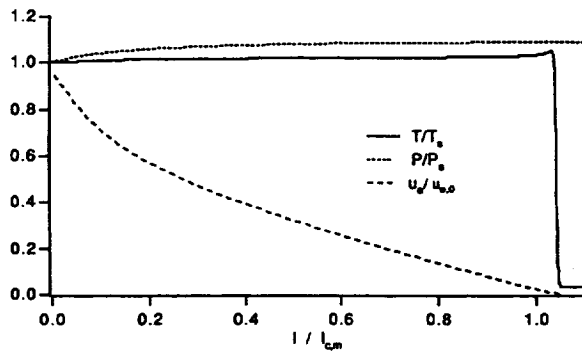
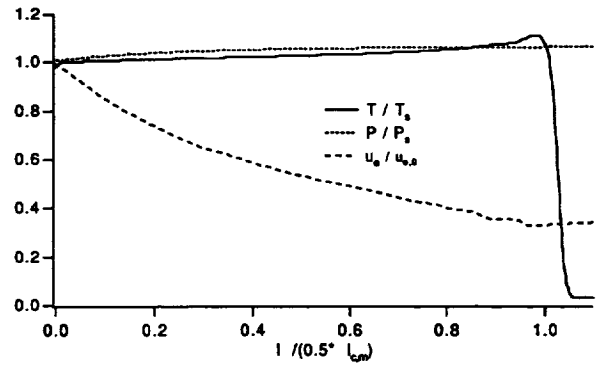Fig. 10   Normalized T, P, and u_c as functions of normalized distance at the limiting flow.

Fig. 11   Normalized T, P, and u_c as functions of normalized distance at a location where $l = (0.5l_{c,m})$.

is about $l_{c,m}/2$ ($t = 0.32$ ms). Even at this early stage, the reduction in u_c can be as high as 60%.

As was discussed in Sec. V.A, the temperature profile in the test gas sample is a very strong function of the shock speed history. At the early stages of the flow the particles are subjected to a large temperature gradient (Figs. 2 and 3), and consequently, the temperature variations in the gas sample in Fig. 11 are much larger than in the limiting flow shown in Fig. 10.

D.   Particle Time of Flight

The inhomogeneity of the test gas sample (seen in Figs. 10 and 11) affects the particle time of flight. As a result, for proper interpretation of shock-tube data, one requires the pertinent information about the flowfield in the test gas sample so that the necessary corrections to the data can be made. For a uniform flow downstream of the shock front, the particle time of flight is given by $t_f = (l/U_s)(\rho_{c,0}/\rho_x) \equiv t_{f0}$. In the case of an inhomogeneous gas sample, it is equal to

$$t_f = \int_0^l \left(\frac{\rho_c}{\rho_x}\right) \frac{dl}{U_s}$$

For strong shocks, Mirels[14] suggests the following correlation for the computations of t_f/t_{f0}:

$$\bar{\tau} = \frac{t_f}{t_{f0}} = \frac{\rho_x}{\rho_{c,0}} \frac{t_f U_s}{l} = \left[2\bigg/\left(\frac{1}{l_{c,m}}\right)\right] \{l_{c,m}[1 - (l/l_{c,m})^{1/2}]^{-1}$$
$$- (l/l_{c,m})^{1/2}\} \tag{7}$$

To visualize the effect of inhomogeneity on the particle time of flight, the nondimensional parameter t_f/t_{f0} is plotted in Fig. 12 as a function of distance from the shock front. This plot is produced for the limiting flow regime using the data for the centerline of the tube. Computations using Eq. (7) are also plotted in the figure. For the plot based on the present computations the velocity data u_c correspond to the centerline grid point. There is a fair agreement between the present computations and the plot based on Mirels' correlation, for $l/l_{c,m} < 0.6$. For $l/l_{c,m} > 0.6$, the data from Mirels' correlation for the particle time of flight are on average about 15–20% higher than the present real-gas solution. At $l/l_{c,m} = 0.9$, the values for t_f/t_{f0} based on the present computations and on Mirels' correlations are 4.2 and 4.5, respectively. In other words, a particle located at the centerline will take about 4.2–4.5 times longer, due to varying thermodynamic conditions in the gas sample, than in a uniform gas sample (if u_c were constant from the shock front to the contact surface).

As was mentioned, the plots in Fig. 12 are for the limiting flow regime. Computations for a location corresponding to point no. 1 on Fig. 4 ($l = 0.5l_{c,m}$) indicate that even at this early stage the ratio t_f/t_{f0} has a value larger than 1.00 and gradually increases with increase in distance as measured from
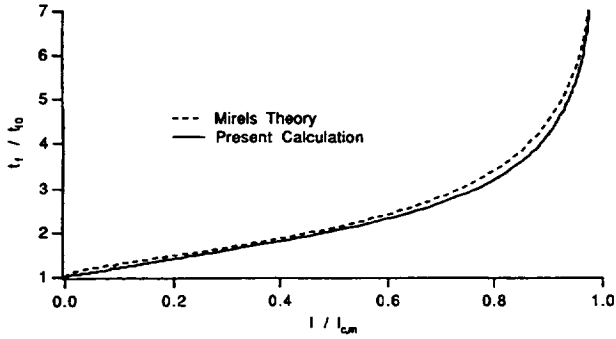
Fig. 12 t_f/t_{fo} as a function of normalized distance at limiting flow.
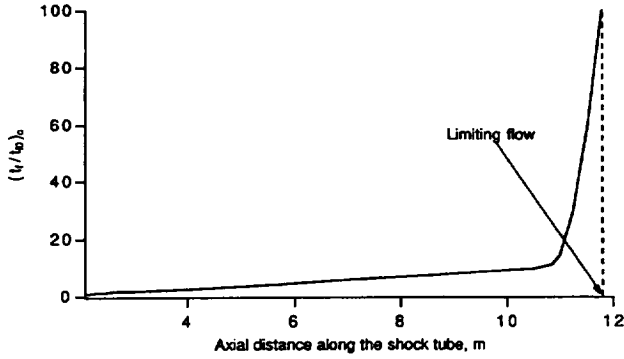

Fig. 13 $(t_f/t_{fo})_c$ as a function of distance along the shock tube.

the shock front. At this location the particle takes about 1.8 times longer than in a uniform flow case to travel a distance equal to $0.5l_{c,m}$.

In Fig. 13, the evolution of the nondimensional parameter $(t_f/t_{fo})_c$ with time can be seen. Here the subscript c denotes the fact that the times of flight are for the distance l_c. The parameter $(t_f/t_{fo})_c$ increases almost linearly as the shock front moves along the shock tube. The maximum value of $(t_f/t_{fo})_c$ is about 100. It must be remembered that strictly speaking, the flow solution has not achieved the true limiting flow condition. It is very near to it and will still require several milliseconds to achieve it. Ultimately, when the limiting flow regime is achieved, the parameter $(t_f/t_{fo})_c$ should become infinite, as Mirels' correlation predicts.

VI.   Discussion

Many important sets of experimental data[19-23] have been acquired in shock tubes and these facilities continue to play a very important role in investigations of chemical kinetics, aerothermodynamics, and space technology. The experimentalists working with shock tubes have been continually searching for improved and accurate techniques for data interpretation. Therefore, whenever new data interpretation tools are available, it is imperative that we assess their capabilities.

In line with this philosophy, the main objective of this study is to demonstrate the usefulness of the present computer code in analyzing the flowfield in shock tubes, providing necessary information about the nonuniformities of the test gas sample to assist the experimentalist in interpretation of shock-tube data. The input conditions for this case are selected so that the basic assumptions made by Mirels also apply to the present flowfield. Using this solution we proceeded to validate this computer code against Mirels' correlations and vice versa. To the best of the authors' knowledge, no other multidimensional CFD solution has been compared with the results obtained from Mirels' correlations.

In most shock-tube experiments the task of data interpretation requires more information about the flowfield than provided by Mirels' correlations.

1) The experimentalist needs to know the thickness and thermal properties of the boundary layer through which the laser beam passes or through which emission measurements are being made.

2) In searching through operating conditions of the shock tube or for an expansion tube, flowfield information behind the contact surface may be required.

3) Flowfield properties of the inhomogeneous gas sample may be required for proper evaluation of particle time of flight. For all of this information the flowfield solution of the shock tube in question will be essential.

Mirels' universal correlations are excellent tools for estimating the test times in shock tubes, especially for the limiting flow regime. However, as we have shown, for correct assessment of the boundary-layer parameters, one requires a detailed flowfield solution of the shock tube. With our present knowledge of real-gas effects, modern CFD techniques, and the availability of supercomputers, it is now possible to provide improved data to experimentalists for proper interpretation of shock-tube data.

VII.   Conclusions

Capabilities of a time-accurate shock-tube flow code have been demonstrated. The boundary-layer parameters, such as δ_u, δ^*, δ_ρ, τ_w (see Appendix), and other shock-tube parameters such as $\bar{\tau}$, have been computed using this code. The parameters such as $\bar{\tau}$ and $l_{c,m}$ agree well with the values computed using Mirels' correlations. However, the boundary-layer thicknesses δ_u, δ_u, and δ^*, do not. The particle time of flight data for the limiting case also show good agreement.

The computations also indicate that flow nonuniformities do exist even at early stages of the shock-tube flow, and consequently, one must make correction for particle time of flight in data taken at those locations. However, to do so one needs to make use of computer codes such as the one presented in this article, since Mirels' work does not provide correlations for cases other than the limiting flow case. Most shock tubes in use are not long enough so that the limiting flow conditions can be achieved. Therefore, in most cases, it is not possible to use Mirels' correlations.

Mirels' correlations and the present shock-tube code have been validated against each other. At the same time, it is concluded that for proper interpretation of shock-tube data, one must make use of a code like the one presented in this article.

Appendix: Mirels' Correlational Formulas

For completeness, Mirels' correlational formulas[12] for laminar boundary layer that have been used in this study are reproduced.

Boundary-layer parameters:

$$\delta_u = y \quad \text{at} \quad \frac{u}{u_e} = 0.99, \qquad (-1)\delta^* = \int_0^\infty \left[\frac{\rho u}{(\rho u)_{e,0}} - 1.0 \right] dy$$

$$(-1)\delta_\rho = \int_0^\infty \left[\frac{\rho}{(\rho)_e} - 1.0 \right] dy, \qquad \tau = \left(\frac{\mu \partial u}{\partial y} \right)_w$$

The boundary-layer parameters with real-gas effects and corrections for variable $\mu\rho$ as published by Mirels[12] are given:

$$\bar{\delta}_u \equiv \frac{\delta_u}{x^{1/2}} \left(\frac{p_1}{p_{st}} \right)^{1/2} \left(\frac{\mu_{st}}{\mu_1} \right)^{1/2} \left(\frac{T_{st}}{T_1} \right)^{1/4}$$

$$= C_e^{0.48} \left[\frac{2p_2/p_1}{M_s W(W-1)} \right]^{1/2} \left[\left(\frac{\mu}{\rho a} \right)_{st} \right]^{1/2}$$

$$\times \left[\eta_u - \left(1 - \frac{W}{p_2/p_1} \right) \int_0^\infty (1 - G)\, d\eta \right] \qquad (A1)$$

$$\bar{\delta}^* \equiv (-1)\frac{\delta^*}{x^{1/2}} \left(\frac{p_1}{p_{st}}\right)^{1/2} \left(\frac{\mu_{st}}{\mu_1}\right)^{1/2} \left(\frac{T_{st}}{T_1}\right)^{1/4}$$

$$= C_\epsilon^{0.37} \left[\frac{2p_2/p_1}{M_s W(W-1)}\right]^{1/2} \left[\left(\frac{\mu}{\rho a}\right)_{st}\right]^{1/2}$$

$$\times \left[(W-1)(\eta - \phi)_\infty + \left(1 - \frac{W}{p_2/p_1}\right)\int_0^\infty (1-G)\,d\eta\right]$$
(A2)

$$\bar{\delta}_\rho \equiv (-1)\frac{\delta_\rho}{x^{1/2}} \left(\frac{p_1}{p_{st}}\right)^{1/2} \left(\frac{\mu_{st}}{\mu_1}\right)^{1/2} \left(\frac{T_{st}}{T_1}\right)^{1/4}$$

$$= C_\epsilon^{0.48} \left[\frac{2p_2/p_1}{M_s W(W-1)}\right]^{1/2} \left[\left(\frac{\mu}{\rho a}\right)_{st}\right]^{1/2}$$

$$\times \left[\left(1 - \frac{W}{p_2/p_1}\right)\int_0^\infty (1-G)\,d\eta\right]$$
(A3)

$$\bar{\tau}_w \equiv (-1)\tau_w x^{1/2}\left(\frac{p_{st}}{p_1}\right)^{1/2}\left(\frac{\mu_{st}}{\mu_1}\right)^{1/2}\left(\frac{T_{st}}{T_1}\right)^{1/4}$$

$$= C_\epsilon^{0.29}\left\{\frac{1}{2}\frac{p_2}{p_1}\left[\frac{M_s(W-1)}{W}\right]^3\right\}^{1/2}\phi''(0)\left[\mu a\left(\frac{\rho a}{\mu}\right)^{1/2}\right]_{st}$$
(A4)

$$\bar{q}_w \equiv q_w x^{1/2}\frac{h_{st}}{h_1}\left(\frac{p_{st}}{p_1}\right)^{1/2}\left(\frac{\mu_{st}}{\mu_1}\right)^{1/2}\left(\frac{T_{st}}{T_1}\right)^{1/4} = C_\epsilon^{0.29}\frac{\chi - 1}{\chi}$$

$$\times \left[\frac{(W-1)}{2W}\frac{P_2}{P_1}M_s\right]^{1/2}\frac{G'(0)}{\sigma^{1/2}}\left[h\left(\frac{\rho a k}{C_p}\right)^{1/2}\right]_{st}$$
(A5)

where

$$C_\epsilon \equiv \frac{\rho_e \mu_e}{\rho_w \mu_w} = \frac{1}{z_2}\frac{T_1}{T_2}\frac{\mu_2}{\mu_1}, \qquad z_2 = \frac{P_2}{\rho_2 R T_2}$$

is the correction factor for variable $\rho\mu$ and $\chi = h_w/h_e$. The parameters $\phi''(0)$, η_α, $\int_0^\infty (1 - G)\,d\eta$, etc., are computed by the following relationships:

$$\phi''(0) = \frac{0.7979}{\varepsilon^{1/2}}(1 + 1.285\varepsilon + 0.3827\varepsilon^2)^{1/4} \qquad (0.1\%)$$
(A6)

$$(\eta - \phi)_\infty = \frac{0.7979\varepsilon^{1/2}}{(1 + 1.099\varepsilon + 0.2376\varepsilon^2)^{1/4}} \qquad (0.2\%) \quad (A7)$$

$$\nu_\alpha = \frac{2.575\varepsilon^{1/2}}{(1 + 0.803\varepsilon + 0.1069\varepsilon^2)^{1/4}} \qquad (0.6\%) \quad (A8)$$

$$\sigma^{1/2}\int_0^\infty (1 - G)\,d\eta = \left[\frac{\varepsilon\phi''(0)}{\varepsilon + 2} + \frac{(\eta - \phi)_\infty}{\varepsilon + 2}\right]$$

$$\times \frac{1 + 0.32\varepsilon}{1 + 0.32\varepsilon\sigma^{0.8}} \qquad (0.3\%)$$
(A9)

$$\frac{G'(0)}{\sigma^{1/2}} = \phi''(0)\left(1 + \frac{\varepsilon}{\varepsilon + 2}\sigma^{0.54}\right) \qquad (0.3\%) \quad (A10)$$

where $\varepsilon \equiv W - 1$ and σ is the Prandtl number. The maximum error is indicated for each expression.

Acknowledgments

References

[1]Payman, W., and Shepherd, W. C. F., "Explosion Waves and Shock Waves: VI. The Disturbance Produced by Bursting Diaphragms with Compressed Air," *Proceedings of the Royal Society of London, Series A: Mathematical and Physical Sciences*, Vol. 186, 1946, pp. 293–321.

[2]Resler, E. L., Lin, S. C., and Kantrowitz, A., "The Production of High Temperature Gases in Shock Tubes," *Journal of Applied Physics*, Vol. 23, No. 12, 1952, pp. 1390–1399.

[3]Hollyer, R. N., Hunting, A. C., Laporte, O., and Turner, E. B., "Luminosity Generated by Shock Waves," *Nature*, Vol. 171, No. 4348, 1953, pp. 395, 396.

[4]Camm, J. C., and Rose, P. H., "Electric Shock Tube for High Velocity Simulation," AVCO Everett Research Lab., Research Rept. 136, Everett, MA, July 1962.

[5]Kantrowitz, A., "Shock Tubes for High Temperature Gas Kinetics," *Energy Transfer in Gases*, edited by R. Stoops, Interscience, New York, 1963, pp. 241–288.

[6]Duff, R. E., "Shock Tube Performance at Low Initial Pressure," *Physics of Fluids*, Vol. 2, No. 2, 1959, pp. 207–216.

[7]Roshko, A., "On Flow Duration in Low-Pressure Shock Tubes," *Physics of Fluids*, Vol. 3, No. 6, 1960, pp. 835–842.

[8]Hooker, W. J., "Testing Times and Contact-Zone in Shock-Tube Flows," *Physics of Fluids*, Vol. 4, No. 12, 1961, pp. 1451–1463.

[9]Mirels, H., "Laminar Boundary Layer Behind a Strong Shock Moving into Air," NASA TN D-291, Feb. 1961.

[10]Mirels, H., "Boundary Layer Growth in Shock Tubes," *Proceedings of the 8th International Symposium on Shock Waves* (Imperial College of Science & Technology, London), Chapman and Hall, London, 1971, pp. 6/1–6/30.

[11]Mirels, H., "Test Time in Low-Pressure Shock Tubes," *Physics of Fluids*, Vol. 6, No. 9, 1963, p. 1201.

[12]Mirels, H., "Correlation Formulas for Laminar Shock Tube Boundary Layer," *Physics of Fluids*, Vol. 9, No. 7, 1966, p. 1265.

[13]Mirels, H., and King, W. S., "Series Solutions for Shock Tube Laminar Boundary Layer and Test Time," *AIAA Journal*, Vol. 4, No. 5, 1966, pp. 782–789.

[14]Mirels, H., "Flow Nonuniformity in Shock Tubes Operating at Maximum Test Times," *Physics of Fluids*, Vol. 9, No. 10, 1966, pp. 1907–1912.

[15]Wuster, W. H., Treanor, C. E., and Williams, M. J., "Non-Equilibrium Radiation from Shock Heated Air Final Report," Calspan-UB Research Center, Buffalo, New York, July 1991.

[16]Sharma, S. P., and Park, C., "Operating Characteristics of a 60 cm and a 10 cm Electric Arc Driven Shock Tube—Part I: The Driver," *Journal of Thermophysics and Heat Transfer*, Vol. 4, No. 3, 1990, pp. 259–265.

[17]Wilson, G. J., Sharma, S. P., and Gillespie, W. D., "Time-Dependent Simulations of Reflected Shock/Boundary Layer Interaction," AIAA Paper 93-0480, Jan. 1993.

[18]Yee, H. C., "A Class of High-Resolution Explicit and Implicit Shock-Capturing Methods," NASA TM 101088, Feb. 1989.

[19]Allen, R. A., Rose, P. H., and Camm, J. C., "Nonequilibrium and Equilibrium Radiation at Super-Satellite Re-Entry Velocities," AVCO Everett Research Lab., Research Rept. 156, Everett, MA, Sept. 1962.

[20]Teare, J. D., Georgiev, S., and Allen, R. A., "Radiation from the Nonequilibrium Shock Front," AVCO Everett Research Lab., Research Rept. 112, Everett, MA, Oct. 1961.

[21]Camm, J. C., Kivel, R. L., Taylor, R. L., and Teare, J. D., "Absolute Intensity of Nonequilibrium Radiation in Air and Stagnation Heating at High Altitudes," AVCO Everett Research Lab., Research Rept. 93, Everett, MA, Dec. 1959.

[22]Sharma, S. P., and Gillespie, W. D., "Nonequilibrium and Equilibrium Shock Front Radiation Measurements," *Journal of Thermophysics and Heat Transfer*, Vol. 5, No. 3, 1991, pp. 257–265.

[23]Sharma, S. P., Gillespie, W. D., and Meyer, S. A., "Shock Front Radiation Measurements in Air," AIAA Paper 91-0573, Jan. 1991.